

# Hierarchical layered titanate microspherulite : formation by electrochemical spark discharge spallation and application in aqueous pollutant treatment

Tang, Yuxin; Gong, Dangguo; Lai, Yuekun; Shen, Yiqiang; Zhang, Yanyan; Huang, Yizhong;  
Tao, Jie; Lin, Changjian; Dong, Zhili; Chen, Zhong

2010

Tang, Y., Gong, D., Lai, Y., Shen, Y., Zhang, Y., Hu, Y. et al. (2010). Hierarchical layered titanate microspherulite: formation by electrochemical spark discharge spallation and application in aqueous pollutant treatment. *Journal of Materials Chemistry*, 20(45).

<https://hdl.handle.net/10356/94054>

<https://doi.org/10.1039/C0JM02005B>

---

© 2010 Royal Society of Chemistry. This is the author created version of a work that has been peer reviewed and accepted for publication by *Journal of Materials Chemistry*, RSC. It incorporates referee's comments but changes resulting from the publishing process, such as copyediting, structural formatting, may not be reflected in this document. The published version is available at: [DOI: <http://dx.doi.org/10.1039/C0JM02005B> ].

*Downloaded on 25 Aug 2022 22:36:57 SGT*

# Hierarchical Layered Titanate Microspherulite: Formation by Electrochemical Spark Discharge Spallation and Application in Aqueous Pollutant Treatment

Yuxin Tang,<sup>a,b</sup> Dangguo Gong,<sup>a</sup> Yuekun Lai,<sup>a,c</sup> Yiqiang Shen,<sup>a</sup> Yanyan Zhang,<sup>a</sup> Yizhong Huang,<sup>a</sup> Jie Tao,<sup>b</sup>  
5 Changjian Lin,<sup>c</sup> Zhili Dong,<sup>\*a</sup> and Zhong Chen<sup>\*a</sup>

*Received (in XXX, XXX) Xth XXXXXXXXXX 200X, Accepted Xth XXXXXXXXXX 200X*

*First published on the web Xth XXXXXXXXXX 200X*

DOI: 10.1039/b000000x

An ultrafast and template-free method to synthesize three-dimensional (3D) hierarchical layered  
10 titanate microspherulite (TMS) particles with high surface area is reported. The synthesis makes use of  
an electrochemical spark discharge spallation (ESDS) process, during which fast anodic reaction on  
titanium surface creates a layer of titanium dioxide that instantly breaks down by the applied electrical  
field into the solution in the form of titanium oxide particles. The spalled particles readily react with  
the heated NaOH electrolyte to form the titanate particles. A typical as-prepared TMS with a diameter  
15 of 0.4~1.5  $\mu\text{m}$  is synthesized by ESDS of Ti foils in 10 M NaOH solution under an applied current  
density of 0.5  $\text{Acm}^{-2}$ , leading to a reaction yield of approximately 0.10~0.15 g per square centimeter of  
exposed Ti foil within 20 min. After hydrogen ion exchange, the surface area can reach as high as  
~406  $\text{m}^2\text{g}^{-1}$ . On the Ti surface, crystalline rutile  $\text{TiO}_2$  nanosheet structure is formed, which is attributed  
to the local exothermic heat caused by the spark discharge. A formation mechanism of the TMS is  
20 discussed based on field emission scanning electron microscopy (FESEM), transmission electron  
microscope (TEM) study and Raman scattering spectroscopy analysis. The as-prepared TMS shows  
excellent adsorption performance compared with a titanate micro-particle (TMP), nanowire (TNW)  
and nanotube (TNT) when methylene blue (MB) and  $\text{Pb}^{\text{II}}$  ions are used as representative organic and  
inorganic pollutants. The mechanism of adsorption has also been discussed.

## Introduction

In recent years, hierarchically structured materials with various morphologies have attracted great attention.<sup>1</sup> Different types of nanostructures, such as column arrays, polyhedron-like particles, belt-  
5 branched, core/shell spheres, and vesicles, have been synthesised using functional materials such as SiO<sub>2</sub>, TiO<sub>2</sub>, SnO<sub>2</sub>, MnO<sub>2</sub>, and carbon. The synthesis methods vary from template-assisted growth to solvothermal or other solution-based, template-free processes.<sup>1,2</sup> The formation of hierarchical structure is generally considered to be a self-assembly process, in which building blocks, i.e., nanoparticles (0D), nanofibers or nanotube (1D), and nanosheets (2D) self-assemble into regular  
10 higher level structures. Many investigations have demonstrated that hierarchical structures could improve the performance of materials in optoelectronic, biomedical, absorption, magnetic applications and energy storage due to their highly porous structure with a large specific surface area.<sup>2-4</sup> In all these cases, controlled synthesis of 3D nanostructure plays an important role to achieve the advanced materials application targets.

15

Layered titanate nanomaterials, traditionally synthesised by alkaline hydrothermal process,<sup>5</sup> have shown excellent properties for ion-exchange, molecular absorption, photoelectricity and wettability contrast.<sup>6</sup> So far, the synthesis of 1D and 2D titanate nanomaterial has been widely investigated. For example, 1D titanate nano- tubes,<sup>6e,7</sup> fibers/wires,<sup>6a</sup> belts,<sup>8</sup> and rods,<sup>9</sup> have been synthesized by  
20 hydrothermal method. The drawbacks of such method include the requirement for high pressure vessel, heating (typically 100~200 °C), and the relatively long processing time (10~120 h),<sup>6d,10</sup> which poses a limit to the productivity and often results in high production cost. Other researchers have used either molten-salt synthesis of TiO<sub>2</sub> mixture at 825 °C for 3 h<sup>8c</sup> or high-temperature oxidation of NaOH coated Ti foils at 800 °C for 1.5 h in the presence of O<sub>2</sub> and H<sub>2</sub>O vapor.<sup>9</sup> The 2D titanate  
25 nanosheets have also been prepared by one step hydrothermal route<sup>11</sup> or a two-step approach involving

the titanate formation and exfoliation.<sup>12</sup> So far it remains a great challenge to produce 3D hierarchically elaborate shape of titanate over multiple scales and the synthesis is usually not straightforward.<sup>3,11,13</sup> Recently, Cao et al.<sup>11</sup> synthesized titanate flowers via a template-assisted approach through hydrothermal reaction between NaOH solution and the mixture of  $\text{TiO}_2$  and  $\text{Zn}(\text{NO}_3)_2 \cdot 6\text{H}_2\text{O}$ . Titanate flowers formed after removing ZnO flower-like nanorods framework. Yoshikawa et al.<sup>14</sup> reported a two-step method combining hydrolysis of titanium tetraisopropoxide with hydrothermal treatment of amorphous  $\text{TiO}_2$  spheres to prepare flower-like titanate nanosheets. Imai's group<sup>3</sup> had explored various kinds of hierarchical ammonium titanate nanosheet morphologies grown in the agar gel medium by a bottom-up route. Mao and co-workers<sup>13</sup> demonstrated the growth of micrometer scale sea-urchin-like structures by an oxidizing  $\text{H}_2\text{O}_2$  assisted-hydrothermal method in autoclave at different temperatures and durations. They proposed a two-stage growth mechanism for the formation of titanate spheres. Self-assembled titanate nanosheets were also synthesized via chimie-douce method by refluxing  $\text{TiO}_2$  powder in 15 M NaOH at 423 K for more than 24 h.<sup>15</sup> Moreover, Xie' group used the Kirkendall effect to construct 3D hollow titanate tubular hierarchical structures via treating  $\text{TiCl}_4$  precursor in other alkaline solutions (e.g., ethylenediamine) at 225 °C for 12 h.<sup>16</sup> Despite the 3D complex structures that have been achieved by these methods, a facile and inexpensive scheme for the controlled morphologies with well defined hierarchical 3D structures is still lacking and will be of great interest to researchers in the field.

So far, the hydrothermal route appears to be most popular for the synthesis of 1D, 2D and 3D titanate materials. The efficacy of the hydrothermal vessel notwithstanding, conventional glassware is more readily accessible to many nanotechnology scientists and chemists and less costly. Some existing approaches require multiple steps or a long processing time to ensure complete reaction,<sup>3-16</sup> e.g., the time taken for the reaction between agar gel with Ti precursor and  $\text{NH}_4\text{OH}$  is one week.<sup>3</sup> Other

methods like molten-salt synthesis<sup>8c</sup> and high-temperature oxidation<sup>9</sup> involve complicated processes and/or high temperature (> 800 °C). All these have posed limitation to the practical application of these materials that have shown excellent performance. It has been well known that TiO<sub>2</sub> porous layer can be formed on Ti foil surface by electrochemical anodization<sup>17</sup> or plasma electrolytic oxidation<sup>18</sup> of Ti foils. Inspired by theses work, we develop a novel one-pot approach to produce highly porous hierarchical 3D titanate micro-spherulite (TMS) particles (surface area exceeds 400 m<sup>2</sup>g<sup>-1</sup>) via a simple, high throughput method employing simultaneously electrochemical anodization and spark discharge of the anodized oxide layer into a reactive solution by carefully adjusting the applied electrical spark parameters in a traditional ambience setup,<sup>17,19</sup> which shown in Fig. 1. Additionally, when used as adsorbent in waste-water treatment, the as-prepared layered titanate TMS exhibits a good ability to remove methylene blue dye and toxic lead ions.

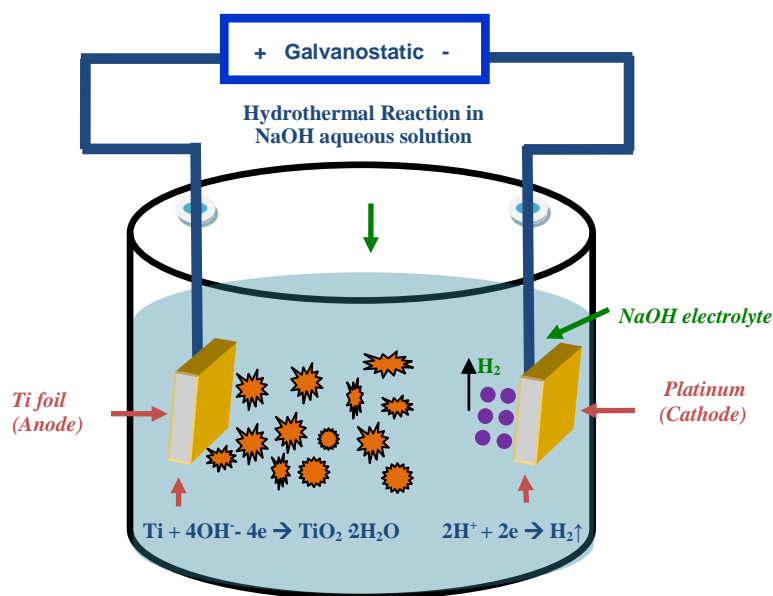


**Fig. 1** Schematic representation of a reaction process by electrochemical spark discharge spallation of a starting Ti foil.

## Experimental

### *Preparation of materials*

TMS particles were prepared from a starting titanium foils (0.25 mm thickness, 99.7% purity  
5 purchased from Aldrich Corporation) via rapid ESDS method in an electrolyte of 10 M sodium  
hydroxide (NaOH) in aqueous solution using a platinum counter-electrode (99% purity Alfa-Aesar  
Corporation, Ward Hill, MA), as shown in Fig. 1. The anodization was conducted in galvanostatic  
mode at a current density ranges from 0.25 to 1.0 Acm<sup>-2</sup> at room temperature (about 25 °C), and the  
distance between two electrodes was 3 cm. To ensure lab safety, the experiments should be carried out  
10 in a fume hood with good ventilation so that any generated gases (e.g., H<sub>2</sub>) can be instantly removed.  
The exposed area of Ti foil was about 2 cm<sup>2</sup> for all the experiments. Prior to the experiment, the  
titanium foil was degreased by alcohol and cleaned by deionized (DI) water. Then it was chemically  
polished by the polishing solution composed of concentrated nitric acid and hydrofluoric acid mixed at  
1:1 proportion by volume. The titanium foil was cleaned again by DI water and dried by N<sub>2</sub> gas before  
15 the experiment. In order to investigate the electrochemical spallation behaviour and the variation of  
solution temperature, the temporal evolutions of anodic voltage and the solution temperature with time  
were obtained by using digital multimeter and thermometer recorder interfaced with a computer  
respectively. After completion of the experiment, grey white precipitates collected from solution was  
centrifuged and washed with DI water until the pH value of the solution was around 8~9. The  
20 hydrogen titanate was obtained by soaking the precipitates in HCl solution (0.1 M) for 3 h, followed  
by washing in DI water and absolute ethanol and drying in air. The process was repeated by 3 times.  
The surface of Ti foil was repeatedly rinsed with DI water and subsequently dried by N<sub>2</sub> gas prior to  
FESEM observation.

### *Sample Characterization*

The morphologies of the as-synthesized TMS particles and Ti surface after anodization were investigated by a field emission scanning electronic microscope (FESEM, JEOL JSM-6340F). A transmission electron microscope (TEM, JEOL JEM-2010) operating at 200 kV was used to characterize the detailed nanostructures. Energy dispersive X-ray analysis was carried out in  
5 attachments in the TEM and FESEM. A Shimadzu 6000 X-ray diffractometer with a Cu K $\alpha$  source was used for phase identification. Nitrogen adsorption/desorption isotherms were measured at 77 K using ASAP2000 adsorption apparatus from Micromeritics. The samples were degassed at 373 K for 4 h under vacuum before analysis. Raman measurements were performed at room temperature in a WITEC confocal spectrometer with a 488 nm excitation laser operated at a low power level (1 mW),  
10 and the Si peak at 520 cm<sup>-1</sup> was used as a reference for the wave number calibration.

### ***Adsorption test***

In order to determine and compare the adsorption performance of the as-synthesized TMS, TMP, TNW and TNT samples, the heavy toxic Pb<sup>II</sup> and methylene blue (MB) were selected. All the adsorption experiments were conducted at stirring condition throughout the test at room temperature  
15 (25 °C) in the dark. For the MB dye, equilibrium adsorption isotherm was determined by concentration variation method. The experiment was carried out with 50 mL of MB solution with varying concentration from 20 to 100 ppm. In each run, 10 mg of adsorbent was added to the solutions. The pH value was within the range of 9.5~10. After 72 h, equilibrium was reached and the equilibrium concentration was measured. The sorption kinetics test was done with 100 mL of MB solution with an  
20 initial concentration of 20 ppm. In each run, 10 mg of the synthesized powder was added. The quantitative determination of the MB concentration in solution at different time intervals was performed by measuring the intensity change absorption peak (at 665 nm) of the sample solution under a Perkin-Elmer UV-Vis-NIR Lambda 900 spectrophotometer.

The Pb<sup>II</sup> exchange isotherm was measured by equilibrating 20 mg of the adsorbents in 50 mL of Pb(NO<sub>3</sub>)<sub>2</sub> having concentration range of 0.1~2.0×10<sup>-3</sup> M for 72 h. The initial pH value of the prepared solutions was adjusted at about 5.0~5.5 during the sorption process to avoid the formation of PbCO<sub>3</sub> or Pb(OH)<sub>2</sub> on the titanate surface. The sorption kinetics was also investigated. 5 mL Pb<sup>II</sup> suspension solution after equilibrating an adsorbent with the solution were collected at 5, 10, 20, 30, 60 and 120 min, respectively. The collected samples was centrifuged and filtered, and the concentrations of Pb<sup>II</sup> were determined by inductively coupled plasma atomic emission spectroscopy (ICP-OES).

## Result and Discussions

### Electrochemical spark discharge spallation behavior

The temporal evolutions of anodic voltage and the solution temperature with time at different current densities are shown in Fig. 2. In the current setup, the applied anodization voltage (27.0~31.5 V, Fig. 2a) is higher than the experimental breakdown voltage of TiO<sub>2</sub> (~25 V) in a 10 M NaOH solution. Therefore, the oxide layer at the electrolyte/oxide interface is electrically broken down and spalled into the solution in the form of small precipitates by the generated spark discharge. The electrochemical spallation behaviour can be explained in the light of the voltage- and temperature-time plots, as follows. At the early stage in Fig. 2a, the dielectric breakdown occurs and the voltage increases linearly with anodization time. The linear increase of the voltage and the galvanostatic oxide thickness can be explained by the well-known high field-assisted ionic transport mechanism.<sup>23</sup> The relationship between the anodic current and the electric field strength across the anodic oxide film is described by

$$I = A \cdot \exp(B \cdot U/d), \quad (1)$$

where I is the ionic current, A and B are electrolytic constants, U is the forming voltage and d is the anodic oxide thickness. During galvanostatic anodization, constant electric field strength (U/d) across the previously formed barrier film is required in order to maintain the given constant current density. When the anodization starts, a TiO<sub>2</sub> oxide layer is formed due to interaction of the surface Ti<sup>4+</sup> ions



with hydroxyl ions ( $\text{OH}^-$ ) in the solution.<sup>17-19</sup> As a consequence, when the oxide thickness increases with time at a constant current density, the voltage across the oxide film increases in order to maintain the current density. This explains the linear increase of the voltage at the beginning as shown in Fig. 2a. Initially, it is found that the higher anode voltage is needed when the anodization is conducted at higher current density, and this trend is changed with the increase of solution temperature. The gradual increase of the solution temperature caused by the exothermic reaction is observed in Fig. 2b. Based on Ohm's law, the total resistance for the anodization system  $R=R_c+R_{a/e}+R_e+R_{c/e}$ , where  $R_c$  is the resistance of the circuit,  $R_{a/e}$  is the resistance of anode/electrolyte interface,  $R_e$  the resistance of electrolyte, and  $R_{c/e}$  the resistance of cathode/electrolyte interface.  $R_{a/e}+R_e$  changes all the time and will influence the total  $R$  during the process. During the spark discharge process,  $R_e$  decreases as the temperature rise accelerates the ionic mobility of the electrolyte, and  $R_{a/e}$  is also decreased due to the spallation and dissolution of compact  $\text{TiO}_2$  layer. Consequently, the anodic voltage ( $=I \cdot R$ ) decreases after reaching the maximum voltage under the constant current density mode. It is also observed that the obvious fluctuation of anode voltage occurs, which is caused by the instantaneous change the total resistance ( $R$ ) and the drastic evolution of gas from the electrodes during the dielectric breakdown.

The electrochemical spark discharge spallation under different current densities generates different amount of heat derived from the exothermic reaction. When the process is conducted at high current density, the solution temperature increases much faster. For example, under lower current density ( $0.25 \text{ Acm}^{-2}$ ), the solution temperature was around  $78^\circ\text{C}$  after 25 min anodization due to the limited heat derived from the anode. When the current density rose to  $0.5 \text{ Acm}^{-2}$  or above, rapid increase in solution temperature ( $\sim 110^\circ\text{C}$ ) was observed. The XRD result (Fig. S1) indicates that the titanate material can be formed at low temperatures ( $\sim 78^\circ\text{C}$ ) under a current density of  $0.25 \text{ Acm}^{-2}$ . The morphologies of the titanate particles formed under different current densities are quite similar, thus we focus on one of them ( $0.5 \text{ Acm}^{-2}$ ) in all subsequent studies.

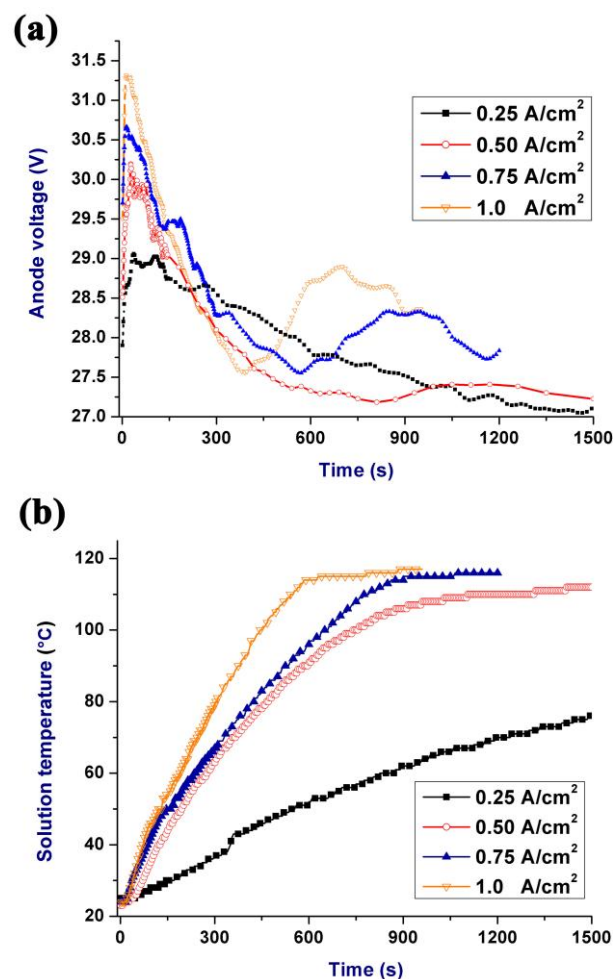


**Fig. 2** Dependence of the anodic voltage (curve a) and solution temperature (curve b) with anodization time in 10 M NaOH solution under different current densities.

## 5 Characterization of the Hierarchical Titanate TMS Materials

The typical FESEM images of the TMS particles and the porous TiO<sub>2</sub> oxide layer on the Ti foil surface after 20 min electrochemical spark discharge spallation (ESDS) processing at a current density of 0.5 Acm<sup>-2</sup> are shown in Fig. 3a and Fig. 3b respectively. The electrolyte turned from clear in the beginning of the process to turbid due to the formation of white precipitates. After the ESDS treatment, the as-  
 10 prepared sodium-hydrogen TMS (NaH-TMS) particles with the diameter ranging from 0.4 μm to 1.5 μm were well dispersed (Fig. 3a). Many fine structures radiating from the core of the spherulite, and they are shown to possess nano-flake structure. The NaH-TMS could be transformed to hydrogen titanate TMS (H-TMS) with the same morphology after acid washing. Energy dispersive X-ray

spectroscopy (EDS) data (Fig. S2) provides the supporting evidence for the transformation from NaH-TMS to H-TMS as there was no Na element in the H-TMS sample. The optical band gap of NaH-TMS and H-TMS are evaluated from Tauc's plot shown in Fig. 4. Their UV-Vis adsorption spectra and digital photos are shown in the insets of Fig. 4. Semiconductors absorb light below a threshold wavelength, the fundamental absorption edge, which is related to the band gap energy ( $E_g$ ) via

$$E_g \text{ (eV)} = 1240 / \lambda_g \text{ (nm)} \quad (2)$$

For a direct band gap transition of titanate materials, the absorption coefficient ( $\alpha$ ) is related to the photon energy ( $E_{ph}$ ) via

$$(E_{ph} \alpha) = B (E_{ph} - E_g)^{0.5} \quad (3)$$

From the Tauc's plot of  $(E_{ph} \alpha)^{0.5}$  vs  $E_{ph}$ , the band gap energy can be determined by extrapolating the linear region. Calculated from the above equations, the onset wavelength of NaH-TMS and H-TMS are about 342 nm and 358 nm, corresponding to the band gap value of 3.62 eV and 3.46 eV respectively. These values are in the same range with previous reports of the titanates.<sup>20</sup> Typical isotherms for nitrogen adsorption and desorption on the surfaces of the as-prepared NaH-TMS and H-TMS conducted at 77 K are shown in Fig. 3c, and the Barrett-Joyner-Halenda (BJH) pore size distribution is shown in the inset. Interestingly, typical type-IV N<sub>2</sub> sorption isotherms with a distinctly increasing step in the middle relative pressures were observed for NaH-TMS and H-TMS, characteristic of mesoporous structure (Fig. 3c).<sup>4</sup> The NaH-TMS has a high Brunauer-Emmett-Teller (BET) surface area of 277.52 m<sup>2</sup>g<sup>-1</sup> with a pore volume of 0.34 cm<sup>3</sup>g<sup>-1</sup>. The average pore size of the NaH-TMS is about 11.8 nm. After acid washing, the H-TMS materials show higher BET surface areas (406 m<sup>2</sup>g<sup>-1</sup>) and larger pore volumes (0.76 cm<sup>3</sup>g<sup>-1</sup>), which come from mesopores of H-TMS possessing a narrow pore size distribution with a peak value of 4.4 nm. The gaps between the thin nano-flakes clearly contribute to the mesoporosity. Fig. 3d shows the crystal structure of the as-prepared TMS. The low diffraction angle at  $\approx 9^\circ$  of the NaH-TMS or H-TMS indicates the product possesses large inter-plane

distance, which is common for layered titanate structures. The broad peaks at  $2\theta=9.2^\circ$  ( $d=9.61$  Å),  $24.6^\circ$  ( $d=3.62$  Å),  $28.5^\circ$  ( $d=3.13$  Å),  $34.9^\circ$  ( $d=2.57$  Å),  $38.8^\circ$  ( $d=2.31$  Å),  $48.3^\circ$  ( $d=1.88$  Å), and  $62^\circ$  ( $d=1.50$  Å) of NaH-TMS correspond well with the (200), (110), (310), (301), (501), (020), and (002) planes of orthorhombic  $\text{H}_2\text{Ti}_2\text{O}_5 \cdot \text{H}_2\text{O}$  (JCPDS No. 47-0124). This type of crystal structure consists of lepidocrocite-type host layers (shown in Fig. 3e) similar to those in the layered  $\text{H}_{0.7}\text{Ti}_{1.825}\Delta_{0.175}\text{O}_4 \cdot \text{H}_2\text{O}$  ( $\Delta$ : vacancy) but with different protons.<sup>7c,21,22</sup> Moreover, thermogravimetric analysis of the TMS sample shown in Fig. S3 implies a strong absorption of water by the titanate: the weight loss of step 1 is due to the evaporation of adsorbed water molecular on the particle surface. The weight loss in step 2 can be attributed to the dehydroxylation of the TMS and the formation of the crystalline  $\text{TiO}_2$ .<sup>21</sup> Based on our measurements, it is reasonable to assign the NaH-TMS and H-TMS as layered  $\text{Na}_x\text{H}_{2-x}\text{Ti}_2\text{O}_5 \cdot \text{H}_2\text{O}$  (Fig. 3e) and  $\text{H}_2\text{Ti}_2\text{O}_5 \cdot \text{H}_2\text{O}$  respectively.

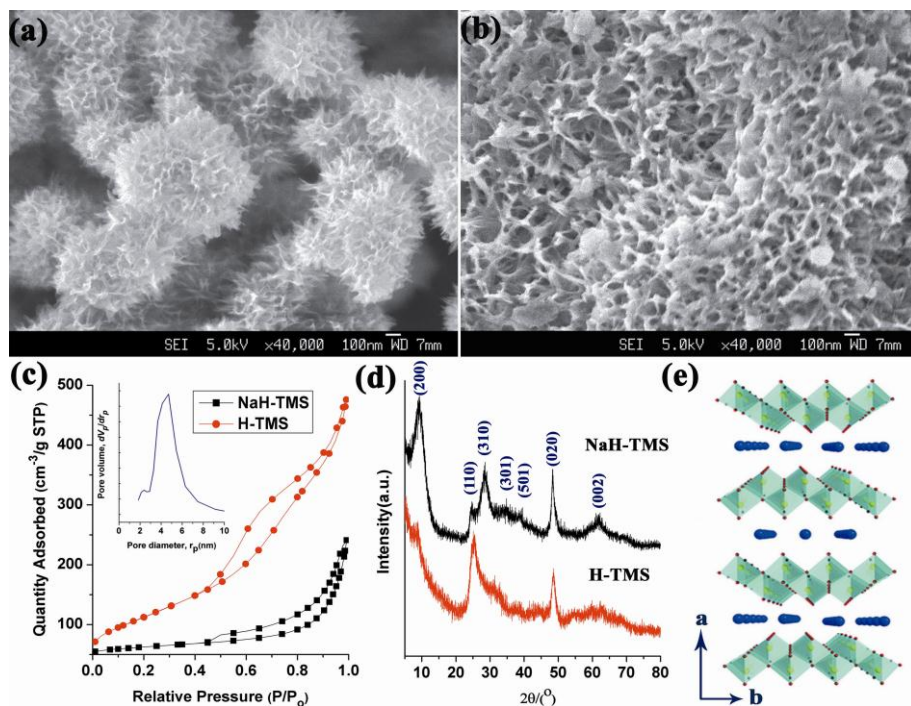


**Fig. 3** FESEM images of the synthesized (a) NaH-TMS; (b) porous  $\text{TiO}_2$  layer left on Ti foil surface by ESDS method in 10 M NaOH solution for 20 min; (c) Isotherm nitrogen sorption of NaH-TMS and H-TMS; (d) XRD patterns of as-prepared NaH-TMS and H-TMS; (e) Polyhedral representation of orthorhombic  $\text{Na}_x\text{H}_{2-x}\text{Ti}_2\text{O}_5 \cdot \text{H}_2\text{O}$ . Interlayer water molecules ( $\text{H}_2\text{O}$ ) are not shown. The dot between the layers is  $\text{Na}^+$  or  $\text{H}^+$ . The samples were anodized at a current density of  $0.5 \text{ Acm}^{-2}$ . The inset in (c) shows a pore volume distribution of H-TMS (BJH desorption).

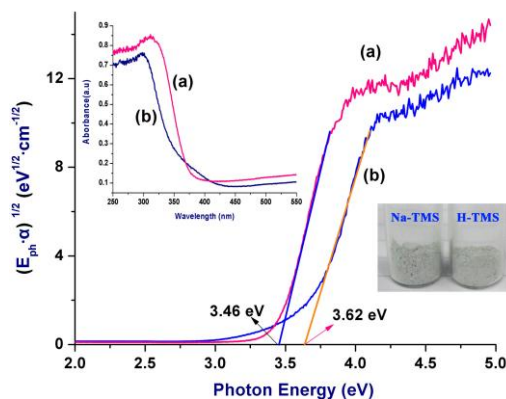


**Fig. 4** Tauc's plots for band gap determination of as-prepared (a) H-TMS and (b) NaH-TMS samples anodized at a current density of  $0.5 \text{ Acm}^{-2}$ ; The insets show their UV-visible diffuse reflectance spectra (left) and the digital photos (right).

5

Transmission electron microscopy (TEM) images shown in Fig. 5 reveal that morphology of the NaH-TMS (Fig. 5a-c) and H-TMS (Fig. 5d-f). The 3D TMS micro-particle consists of individually 2D titanate flakes at nano-scale, centred from the core like a star (Fig. 5b) forming a hierarchical morphology. The insets of Fig. 5b and Fig. 5e are the electron diffraction patterns of NaH-TMS and H-TMS spheres respectively. Diffraction rings were observed since the samples were polycrystalline with the nano-flakes radiating outwards. The three diffraction rings are indexed as coming from the three intensive (110), (310), and (020) diffraction planes for the orthorhombic NaH-TMS, while only two sharp diffraction rings corresponding to the (110) and (020) planes of H-TMS were observed. These results are constant with the XRD results (Fig. 3d). EDS analysis shown in insets of Fig. 5c and Fig. 5f suggests that the NaH- and H-TMS are composed of Na/Ti/O and Ti/O individually while Cu element comes from the copper grid. FESEM-EDS result in Fig. S2 further verifies the elemental information. Based on the fringes in the high-resolution TEM image of the NaH-TMS in Fig. 5c, the interlayer distance of layered structure is ca. 0.74 nm. It is interesting to note that the morphology of H-TMS shown in Fig. 5d is similar to those of the Fig. 5a after acid washing. The displayed interlayer distance for H-TMS is lower and close to 0.70 nm (Fig. 5d), which is consistent with the literature reports.<sup>11,13,15,21</sup> Moreover, the other two fringes with interlayer distances of 0.22 and 0.35 nm in the nano-flakes were observed in Fig. 5f. These three values correspond to the spacing of the (200), (501),

and (110) planes of a lepidocrocite  $\text{Na}_x\text{H}_{2-x}\text{Ti}_2\text{O}_5 \cdot \text{H}_2\text{O}$  respectively. It is noted that the interlayer distance measured from TEM image is smaller than that obtained from XRD measurement. This deviation is caused by the dehydration of the samples in ultrahigh vacuum during the TEM observation.<sup>6d,11,21</sup> The plane view of nano-flakes shown in Fig. 5f and Fig. S4 reveals that the individual flakes consist of tapered ends on the flat plane. Furthermore, the nano-flake is mostly crystalline with the presence of tiny amorphous structure at the ends (Fig. S4b).

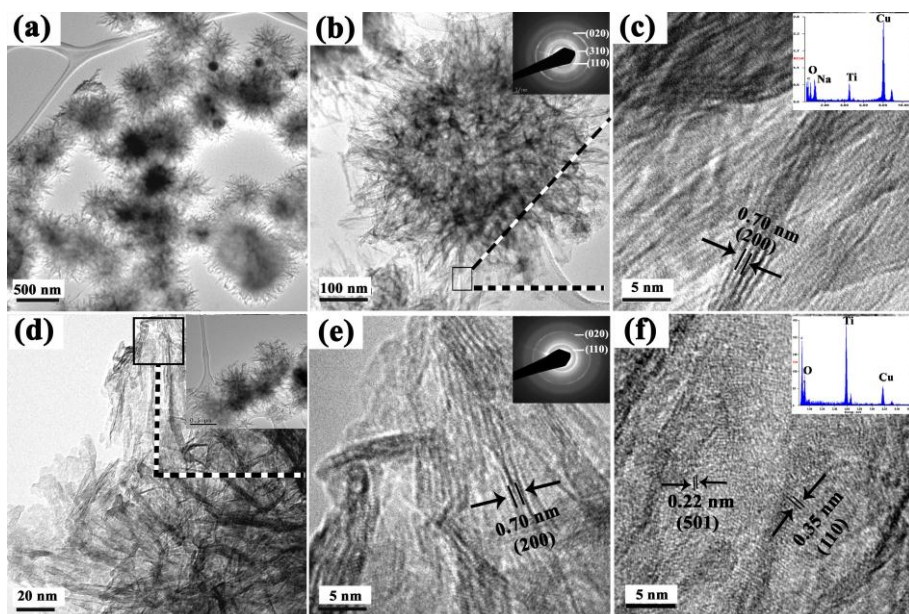
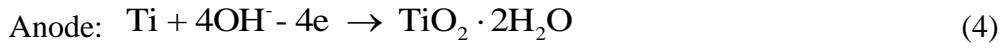


**Fig. 5** TEM image of the fabricated (a) NaH-TMS; (b) individual NaH-TMS anodized under a current density of  $0.5 \text{ A cm}^{-2}$ . The inset shows the corresponding electron diffraction pattern; (c) HRTEM of selected square area in (b). The inset provides the EDS spectra; (d) TEM image of H-TMS nano-flakes. The inset shows the morphology of the H-TMS particles; (e) Enlarged view of the selected area in (d). The inset shows the corresponding electron diffraction pattern; (f) The plane view of the H-TMS flakes. The inset displays the EDS spectra.

## Formation Mechanism

To understand the formation process of the TMS, FESEM observation was carried out on both the powders and the Ti foil surface after different anodization time. The morphological evolution process with time is shown in Fig. S5 and Fig. S6 respectively. The dependence of anodic voltage and the solution temperature with time at a current density of  $0.5 \text{ Acm}^{-2}$  were shown in Fig. 2. Additionally, a series of the powder morphology evolution is shown by TEM in Fig. 6. The Raman scattering spectra (Fig. 7) are also provided to understand the crystal structure evolution with processing time.

When the spark discharge starts, the oxide layer is formed at the electrolyte/oxide interface via



Then the layer is electrically broken down and spalled into the solution at relatively high-voltage electrolyzing oxidation process. Simultaneously, a rapid evolution of hydrogen in the form of strong bubbling occurs at the cathode via:



This ESDS process induces the formation of crystalline  $\text{TiO}_2$  structure, which is triggered by the local exothermic heat caused by the vigorous spark discharge. This is supported by the results of the Raman spectra shown in Fig. 7. The bands located at 144, 198, 398, 515,  $640 \text{ cm}^{-1}$  of the precipitation collected from the solution belong to Raman ( $\text{A}_{1\text{g}} + 2\text{B}_{1\text{g}} + 3\text{E}_{\text{g}}$ ) active modes of the anatase (Fig. 7a, 2 min), and the two fringes with distances of 0.35 nm and 0.46 nm correspond to the spacing of the (011) and (002) planes of anatase  $\text{TiO}_2$  are also observed in Fig. 6b. It was observed that the precipitates possess a microscale spherical core. But on the outer layer of the precipitates, there exist many radiating fine structures with high porosity (Fig. 6a, Fig. S5a-d). With time, the crystal structure of the precipitates changes from anatase (Fig. 7a, 2 min) to mixed anatase/titanate (Fig. 7a, 2.5 min) and mixed rutile/titanate (Fig. 7a, 3 min) before complete conversion to titanate. This implies that the spalled particles were initially anatase phase, and then became rutile after  $\sim 3$  minutes. On the other



hand, the surface layer left on the Ti foil consists of anatase and rutile in the initial stage (Fig. 7b, 2~5 min) and changes to rutile-only later.

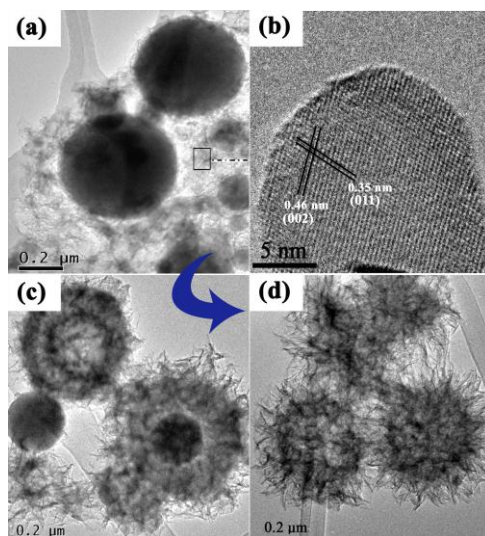
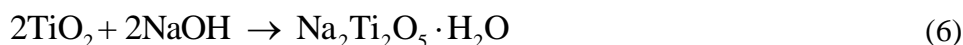


**Fig. 6** TEM images of (a-b), (c), (d) powders samples taken at 2, 10 and 20 min under a current density of  $0.5 \text{ Acm}^{-2}$  respectively. (b) HRTEM image of the selected area in (a).

When the electrolyte temperature increases, hydrothermal reaction of the spalled  $\text{TiO}_2$  particles begins. Strictly speaking, the conditions are not exactly the same as the ones of a hydrothermal reaction (e.g. no high pressure is present in the ESDS process). “Hydrothermal-like” might be more precise to describe the reaction. The reaction also changes the morphology and crystal structure of the spalled particles. The reaction takes place in solution based on the following reaction:



In Fig. 7a, the broad Raman bands located near 188, 280, 389, 447, 705, and  $905 \text{ cm}^{-1}$  belong to titanate structure formed after anodization for 4~5 min. These bands remain the same with prolonged treatment duration up to 20 min. The starting titanate formation temperature in the solution was found to be around  $60^\circ\text{C}$ , which agrees with Kim’s previous report.<sup>24</sup> The titania-titanate transformation has resulted in the spherulite type of titanate particles consisting of radiating nano-flakes. For example, the titania micro-spherulite (Fig. 6a) formed at 2 min has transformed to porous spherulite structure with nano-flakes at 10 min (Fig. 6c) due to the hydrothermal-like reaction. As the reaction proceeds (20



min), the retrieved particles almost completely consist of nano-flakes (Fig. 6d). It was also observed that the average size of precipitates decreases as the reaction proceeds, as shown by the FESEM images of powders collected at different times (Fig. S5). This is likely due to the decrease of the breakdown thickness of the  $\text{TiO}_2$  layer in the heated solution where the voltage applied to the dielectric layer ( $=I \cdot R_{a/e}$ ) decreases. The applied voltage curve conducted at  $0.5 \text{ A cm}^{-2}$  decreases to a steady state in Fig. 2a largely because of the decrease of the dielectric layer voltage.

A layer of crystalline  $\text{TiO}_2$  was formed on the Ti foil surface. Its morphology evolved as shown in Fig. S6. As a result of the spark discharge, the dense oxide layer starts to spall and dissolve, and the Ti surface becomes rougher with time. More detailed examination shows that numerous cracks or pores were formed on the Ti surface (Fig. S6c-e). As the reaction progresses, the increase in temperature resulted in accelerated anodic dissolving  $\text{TiO}_2$  films and the formation of nanosheet structures on the Ti surface (Fig. S6i-n). Since the  $\text{TiO}_2$  layer is continually broken into the solution due to the spark discharge, the surface layer always consists of the freshly formed  $\text{TiO}_2$ . Thus there is not enough time for the chemical reaction between the  $\text{TiO}_2$  and the NaOH solution to occur on the surface of the Ti foil. As a result, no titanate phase was found on the Ti surface (Fig. 7b). The increase of the discharge temperature on the Ti foil surface has promoted the phase transformation of the anodized  $\text{TiO}_2$  layer from anatase to rutile. The Raman spectra in Fig. 7b shows surface layer consists of the anatase and rutile  $\text{TiO}_2$  at the beginning (2~5 min), and then this crystal structure changes completely to rutile  $\text{TiO}_2$  later (10~30 min). The crystalline phase of the spalled particles followed the same sequence (Fig. 7a). Despite of the difference in the starting phase of  $\text{TiO}_2$ , the same titanate phase forms after reaction with high concentration NaOH (Fig. 7a). Our results agree with previous reports that all polymorphs of  $\text{TiO}_2$  (anatase, rutile, brookite, or amorphous) can be transformed to the titanate under alkaline hydrothermal conditions.<sup>[6d,10]</sup>

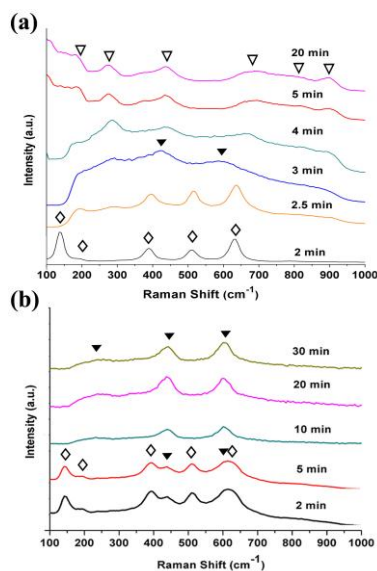


**Fig. 7** Raman spectra of (a) the precipitates collected from the solution after 2, 2.5, 3, 4, 5, 20 min anodization; (b) the TiO<sub>2</sub> layer generated on Ti foil after 2, 5, 10, 20, 30 min anodization (◇--- anatase; ▼--- rutile; ▽---titanate).

On the basis of the experimental results, we propose the followings as the formation mechanism of the hierarchical titanate microspherulite in the solution and TiO<sub>2</sub> nanosheet structure on the Ti foil surface. The whole process is through a synergistic effect of electrochemical spallation and hydrothermal-like reaction, as illustrated in Fig. 8. In the first stage (I), fast anodic reaction on titanium surface creates a layer of titania that instantly breaks down under the applied electrical field into the solution in the form of anatase titania particles (Fig. 7a-2 min, Fig. S5a~b). From the TEM image (Fig. 6a) and SEM image (Fig. S5a-b), it is observed that the titania particle possesses porous surface features. This would facilitate rapid reaction with the NaOH solution. At the same time, numerous small micro-pores (Fig. S6c~e) are formed on Ti foil surface. In the second stage (II), at a relatively higher solution temperature (60 °C, 5 min), the porous spalled particles readily react with the heated NaOH electrolyte to form the titanate particles (Fig. 7a, 5~20 min) in stage (II)-(a), and the hierarchical porous structure (Fig. 6c-h) is gradually derived from the titania precipitate (Fig. 6a). The formation of TMS is ultra fast because the spalled particles can be heated up to extremely high temperature by the spark discharge. It has been reported that spark discharge can cause local temperature to reach several

thousand Kelvin (K),<sup>[18]</sup>. Such a condition is unmatched by any existing methods for titanate formation, which typically take much longer time (12-48 h) for the reaction to complete.<sup>[6, 15]</sup> Using the reflux method, a similar morphology of flower-like titanate particles has been reported.<sup>[15]</sup> However, the surface area ( $\sim 224 \text{ m}^2 \text{ g}^{-1}$ ) was lower than our TMS and the reaction took days to complete.<sup>[15]</sup> In the stage (II)-(b), the micro-pores in the oxide layer on Ti surface turns into nanosheet structure (Fig. S6i-n) as a result of dissolution in the high concentration alkaline solution. This is the first report that crystalline  $\text{TiO}_2$  nanosheet is formed at a low applied voltage (around 30 V) compared to the reported high voltage micro-arc oxidation (100~500 V).<sup>18b-c</sup>

The reported synthesis method is different from all known approaches to form titanate nanostructures. A unique advantage of the current method lies in its high throughput at a simple ambient setup, while most of the reported methods require much longer processing time. The reaction yield of the current method was 0.10~0.15 g TMS per  $\text{cm}^2$  of Ti foil for only 20 min processing at a current density of  $0.5 \text{ A cm}^{-2}$ . The production yield can be easily scaled up by increasing the exposed Ti surface area and the current density. The specific surface area clearly exceeds any reported values of titanate materials (e.g., nano-tubes, wires, etc.) prepared by hydrothermal method so far.

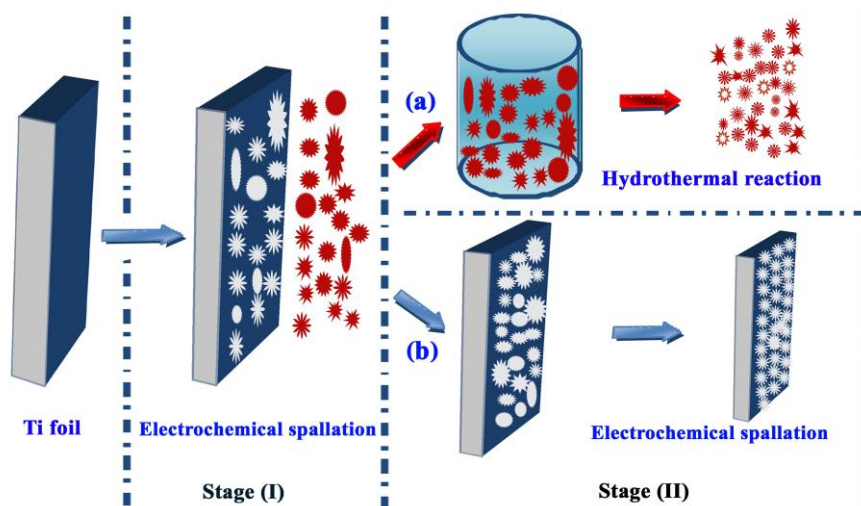


**Fig. 8** Schematic illustration of the formation process for TMS and  $\text{TiO}_2$  nanosheet structure. Stage I: the formation of  $\text{TiO}_2$  particle and  $\text{TiO}_2$  oxide layer by anodization and spallation of Ti foils; stage II:

a) The formation of TMS in the solution by hydrothermal-like process; b) The formation of  $\text{TiO}_2$  porous nanosheet on Ti foil surface.

## 5 Evaluation of the Adsorption Properties

Materials with layered crystal structure, such as titanates and niobates, could be used as adsorbents or catalysts for the removal of organic and inorganic pollutants in waste water. Very recently, the 1D-titanate nanofibers<sup>6a</sup> and nanotubes<sup>6c,25</sup> showed excellent adsorption of organic molecules and radioactive toxic metal ions.<sup>6d</sup> Divalent lead ( $\text{Pb}^{\text{II}}$ ), one of the metals that have the most damaging effects on human health, can cause damage to the central nervous system and dysfunction to the kidneys and immune system of human beings, especially for children.<sup>26</sup> As an example of potential applications, the as-obtained micro-scale 3D-TMS was evaluated for adsorption of toxic heavy metal ions  $\text{Pb}^{\text{II}}$  and methylene blue (MB), a common organic dye in the textile industry. For comparison, we also prepared trititanate micro-particle (TMP) via pyrosynthesis, titanate nanowire (TNW) and titanate nanotube (TNT) by hydrothermal approach. All these samples for the adsorption experiments are without acid washing. The experimental condition and morphology of the prepared TMP, TNW and TNT are shown in Fig. S7. Fig. 9 and Fig. 10 illustrate the absorption performances of different adsorbents for MB and  $\text{Pb}^{\text{II}}$  in aqueous solutions. The as-prepared 3D TMS stands as the best with high removal capacity and adsorption rate of MB compared to TNW, TNT and TMP. TMS can remove 75% MB from the solution in 5 min (Fig. 9a, Fig. S8). After 12 h, it completely removed the MB (Fig. 9b). We estimate that 1.0 g as-prepared TMS can remove about 236.2 mg MB (Table 1, Fig. S9) based on experimental saturate sorption capacity. The sorption capacity of TMS is slightly larger than the corresponding capacity for titanate TNT ( $232.2 \text{ mg g}^{-1}$ , Table 1) and much higher than the ones by the TMP and TNW. The removal capacity was significantly higher than what was reported for a 3D hierarchical titanate spheres.<sup>3,15</sup> The TMS also shows excellent adsorption performance of  $\text{Pb}^{\text{II}}$  ions (Fig. 10). Similar to the adsorption rate of MB, the adsorption of  $\text{Pb}^{\text{II}}$  onto TMS was the fastest. The

TMS was able to remove  $\text{Pb}^{\text{II}}$  from the solution almost completely in less than 10 min, as evidenced by the concentration decrease from  $120.5 \text{ mgL}^{-1}$  ( $C_0$ ) to less than  $0.5 \text{ mgL}^{-1}$  at room temperature (Fig. 10a). In addition, the as-prepared TMS possesses excellent adsorption capacities of  $\text{Pb}^{\text{II}}$  toxic ion. The plateau saturation capacities based on the isotherm curves in Fig. 10b are  $0.56 \text{ mmol g}^{-1}$  for TMP,  $2.41 \text{ mmol g}^{-1}$  for TMS,  $2.60 \text{ mmol g}^{-1}$  for TNT and  $2.62 \text{ mmol g}^{-1}$  for TNW titanate materials (Table 1). The capacity of TMS is greater than TMP and comparable with the 1D nanostructure titanate (TNT, TNW).

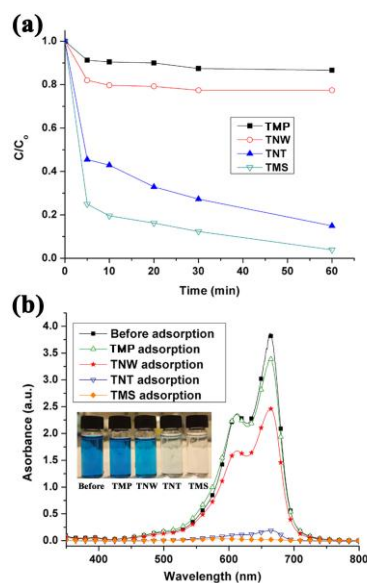


**Fig. 9** (a) Adsorption MB (20 ppm, 50 mL) by TMP, TNW, TNT, and TMS.  $C_0$  (ppm) is the initial concentration of the MB solution and  $C$  (ppm) is the concentration of that at different intervals during the adsorption. (b) Comparison of the absorption spectra of the MB solution (20 ppm, 50 mL) before and after 12 h adsorption and in the presence of TMP, TNW, TNT and TMS. The amount of adsorbent is 10 mg, and photographs showing the solution color are, from left to right, before adsorption, TMP, TNW, TNT and TMS.

**Table 1.** BET surface area and removal capacity of different absorbent samples

Absorbent samples	BET surface area [ $\text{m}^2\text{g}^{-1}$ ]	Experimental capacity for MB [ $\text{mg g}^{-1}$ ]	Experimental capacity for $\text{Pb}^{\text{II}}$ [ $\text{mmol g}^{-1}$ ]
TMP	1.07	$80.8 \pm 7.4$	$0.56 \pm 0.03$
TNW	13.82	$94.6 \pm 4.5$	$2.62 \pm 0.06$
TNT	157.63	$232.2 \pm 11.0$	$2.60 \pm 0.05$
TMS	277.52	$236.2 \pm 10.3$	$2.41 \pm 0.06$

Comparing the performance among the four types of titanate in MB and  $\text{Pb}^{\text{II}}$  adsorption, we believe that the adsorption mechanism are different, which has resulted in the difference in the observed removal capacity. MB is cationic dye; the electrostatic force between the adsorbent and the MB ions

plays an important role in its adsorption capacity. To verify this, we performed Zeta potential measurement of the TNT in different pH values (Fig. S10a) and their corresponding adsorptions of an initial concentration of 20 ppm MB solution are shown in Fig. S10b. The highest MB dye removal occurs at pH 9.5~10 when the titanate surface is most negatively charged. Varying the solution pH affects the adsorption; there was very little MB adsorption when pH=1 (Fig. S10b). Therefore, all the other adsorption performance of titanate materials was performed at pH 9.5~10. The data in Table 1 suggests that the adsorption capacity increases with increasing surface area. It was suggested that MB molecules might be trapped into the interlayer space of the titanate by exchanging with cation ions.<sup>3</sup> However since MB is a larger molecule, we do not expect such an exchange would only occur at sites near the particle surfaces. In other words, the MB adsorption capacity is highly sensitive to the surface area. Therefore it is not surprising that the TMS sample with the hierarchical porous structure as described earlier gives rise to the highest MB adsorption rate and capacity (Fig. 9 and Table 1).

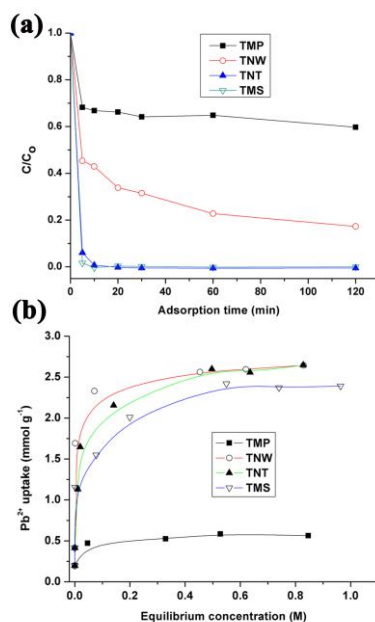
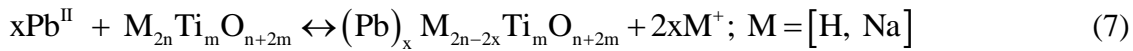


**Fig. 10** Comparison of (a) adsorption rate and (b) adsorption isotherms of Pb<sup>II</sup> ions by TMP, TNW, TNT and TMS.  $C_0$  (120.5 mgL<sup>-1</sup>) is the initial Pb<sup>II</sup> concentration, and  $C$  the concentration at different intervals during the test.

The Pb<sup>II</sup> adsorption by the titanates is through ion-exchange which was evidenced by XRD and Raman measurements,<sup>6a, 6d, 27</sup> i.e., the Pb<sup>II</sup> cations replace the protons or Na<sup>+</sup> via the following reaction:



The cation exchange capacity (CEC= $\text{mol}_{\text{Na,H}}/\text{M}_{\text{w(titanate)}}$ ) of titanate material is mainly depended on the exchange-able sites in the adsorbent. It was found that the exchange capacities of TMS, TNW and TMP are high and comparable, but the one for the TMP is much lower (Table 1). The poor sorption performance of TMP is due to its large particle size which effectively hinders the cation diffusion during the exchange process. As shown in Fig. S7, the particle size of the TMP is around 1~2  $\mu\text{m}$ . In comparison, the TMS sample also has large particle size, but its hierarchical porous structure facilitates the exchange reaction extending to large number of exchangeable sites.

In addition to the morphological reason, the crystal structure may also play an role in the adsorption performance.<sup>6a,27a</sup> The TMP ( $\text{Na}_2\text{Ti}_3\text{O}_7$ ) synthesized by high temperature solid state reaction has a different crystal structure with the one by low temperature solution process. The former has a theoretical cation exchange capacity  $6.62 \text{ mmol g}^{-1}$ , which is lower than the one for TMS ( $\text{Na}_{2-x}\text{H}_x\text{Ti}_2\text{O}_5$ ,  $9.05 \text{ mmol g}^{-1}$ ). Therefore, the surface area and the crystal structure are the main factors that give rise to the excellent adsorption rate and capacity of the TMS particles. Compared with the titanate TMP, TNW and TNT, the TMS has the fastest adsorption rate which is clearly related to its high surface area. There it is the most efficient adsorbent in terms of sorption kinetics for removal of the MB organic dye and Pb<sup>II</sup> heavy metal ions from contaminated water. In addition, as the size of the TMS sample is of the order of micro-meter, the particles will not easily agglomerate. The recovery of the used particles will be much easier than nanoparticles. From practical application point of view, our synthesized TMS also enjoys a clear advantage in terms of production and operation cost.

## Conclusion

We have successfully developed a fast and facile synthesis of 3D TMS with a high specific surface area by a low-cost and simple ESDS method in alkaline solution at an ambient setup. The formation process is led by the concurrent anodic reaction oxidation and the electrical breakdown of the formed oxide layer into the electrolyte in precipitate form. The spallation is driven by continuous spark discharge that simultaneously heat up the solution. The  $\text{TiO}_2$  precipitates then react immediately with the heated NaOH solution to form the TMS particles. The as-prepared TMS powders show excellent ion-exchange ability and high adsorption rate with toxic  $\text{Pb}^{\text{II}}$  ion and the MB dye due to its specific hierarchical structure and crystal structure. The current work creates a novel route to synthesis titanate superstructures with unique morphologies and complex hierarchies at micro- and nanoscale in short processing time. We expect a wide range of applications for this type of materials in photocatalysis and energy storage when excellent functionality and large surface area are essential.

## Acknowledgements

The authors thank the National Research Foundation of Singapore Government (grant MEWR651/06/160) for the financial support of the work. Technical assistance from Prof. T.-T. Lim, Mr. K.-H. Goh, Ms. Jun Guo, and Mr. Lizhi Zhang are gratefully acknowledged. The authors would like to thank the anonymous reviewers for their constructive comments and suggestions which have helped us to improve the discussion of the formation mechanism of TMS.

## Notes and references

<sup>a</sup> School of Materials Science and Engineering, Nanyang Technological University, 50 Nanyang Avenue, Singapore 639798, Singapore; E-mail: aszchen@ntu.edu.sg, zldong@ntu.edu.sg; Fax: +65 6790 9081; Tel.: +65 6790 4256, +65 6790 6727

<sup>b</sup> College of Material Science and Technology, Nanjing University of Aeronautics and Astronautics, 29 Yudao Street, Nanjing 210016, China.

<sup>c</sup> State Key Laboratory of Physical Chemistry of Solid Surfaces and College of Chemistry and Chemical Engineering, Xiamen University, Xiamen 361005, China.



† Electronic Supplementary Information (ESI) available: Additional data for materials characterization and degradation performance. See DOI: 10.1039/b000000x/

- 1 J. S. Hu, L. S. Zhong and W. G. Song, L. J. Wan, *Adv. Mater.* 2008, **20**, 2977.
- 2 (a) Y. Li, T. Sasaki, Y. Shimizu and N. Koshizaki, *J. Am. Chem. Soc.*, 2008, **130**, 14755; (b) C. Xue, J. Wang, B. Tu and D. Zhao, *Chem. Mater.*, 2009, **22**, 494; (c) Y. Q. Dai, X. F. Lu, M. McKiernan, E. P. Lee, Y. M. Sun and Y. N. Xia, *J. Mater. Chem.*, 2010, **20**, 3157; (d) S. H. Sun, G. W. Meng, G. X. Zhang, J. P. Masse and L. Zhang, *Chem. Eur. J.*, 2007, **13**, 9087; (e) D. Gu, H. Bongard, Y. H. Deng, D. Feng, Z. X. Wu, Y. Fang, J. J. Mao, B. Tu, F. Schuth and D. Y. Zhao, *Adv. Mater.*, 2010, **22**, 833.
- 3 Y. Takezawa and H. Imai, *Small*, 2006, **2**, 390.
- 4 H. J. Liu, X. M. Wang, W. J. Cui, Y. Q. Dou, D. Y. Zhao and Y. Y. Xia, *J. Mater. Chem.*, 2010, **20**, 4223.
- 5 (a) T. Kasuga, M. Hiramatsu, A. Hoson, T. Sekino and K. Niihara, *Langmuir*, 1998, **14**, 3160; (b) T. Kasuga, M. Hiramatsu, A. Hoson, T. Sekino and K. Niihara, *Adv. Mater.*, 1999, **11**, 1307.
- 6 (a) D. J. Yang, Z. F. Zheng, H. Y. Zhu, H. W. Liu and X. P. Gao, *Adv. Mater.*, 2008, **20**, 2777; (b) A. Riss, M. J. Elser, J. Bernardi and O. Diwald, *J. Am. Chem. Soc.*, 2009, **131**, 6198; (c) H. Y. Niu, J. M. Wang, Y. L. Shi, Y. Q. Cai and F. S. Wei, *Microporous Mesoporous Mat.*, 2009, **122**, 28; (d) D. V. Bavykin, J. M. Friedrich and F. C. Walsh, *Adv. Mater.*, 2006, **18**, 2807; (e) Y. K. Lai, Y. C. Chen, Y. X. Tang, D. G. Gong, Z. Chen and C. J. Lin, *Electrochem. Commun.*, 2009, **11**, 2268.
- 7 (a) X. M. Sun and Y. D. Li, *Chem. Eur. J.*, 2003, **9**, 2229; (b) Q. Chen, W. Z. Zhou, G. H. Du and L. M. Peng, *Adv. Mater.*, 2002, **14**, 1208; (c) R. Z. Ma, Y. Bando and T. Sasaki, *Chem. Phys. Lett.*, 2003, **380**, 577; (d) C. C. Tsai and H. S. Teng, *Chem. Mater.*, 2004, **16**, 4352; (e) Y. Suzuki and S. Yoshikawa, *J. Mater. Res.*, 2004, **19**, 982.
- 8 (a) H. Y. Zhu, Y. Lan, X. P. Gao, S. P. Ringer, Z. F. Zheng, D. Y. Song and J. C. Zhao, *J. Am. Chem. Soc.*, 2005, **127**, 6730; (b) T. Zhang, Q. Chen and L. M. Peng, *Adv. Funct. Mater.*, 2008, **18**, 3018.
- 9 Z. Liu, T. Yamazaki, Y. Shen, D. Meng, T. Kikuta and N. Nakatani, *J. Phys. Chem. C*, 2008, **112**, 4545.
- 10 R. A. Doong and I. L. Kao, *Recent patents on nanotechnology*, 2008, **2**, 84.
- 11 J. Q. Huang, Z. Huang, W. Guo, M. L. Wang, Y. G. Cao and M. C. Hong, *Cryst. Growth Des.*, 2008, **8**, 2444.
- 12 (a) T. Sasaki and M. Watanabe, *J. Am. Chem. Soc.*, 1998, **120**, 4682; (b) T. Sasaki, Y. Ebina, Y. Kitami and M. Watanabe, T. Oikawa, *J. Phys. Chem. B*, 2001, **105**, 6116; (c) N. Miyamoto, K. Kuroda and M. Ogawa, *J. Mater. Chem.*, 2004, **14**, 165; (d) T. Gao, H. Fjellvag and P. Norby, *J. Phys. Chem. B*, 2008, **112**, 9400; (e) J. H. Choy, H. C. Lee, H. Jung and S. J. Hwang, *J. Mater. Chem.*, 2001, **11**, 2232.
- 13 Y. B. Mao, M. Kanungo, T. Hemraj-Benny and S. S. Wong, *J. Phys. Chem. B*, 2006, **110**, 702.
- 14 J. Jitputti, T. Rattanavoravipa, S. Chuangchote, S. Pavasupree, Y. Suzuki and S. Yoshikawa, *Catal. Commun.*, 2009, **10**, 378.
- 15 C. W. Peng, T. Y. Ke, L. Brohan, M. Richard-Plouet, J. C. Huang, E. Puzenat, H. T. Chiu and C. Y. Lee, *Chem. Mater.*, 2008, **20**, 2426.
- 16 C. Wu, L. Lei, X. Zhu, J. Yang and Y. Xie, *Small*, 2007, **3**, 1518.

- 17 (a) G. K. Mor, O. K. Varghese, M. Paulose, K. Shankar and C. A. Grimes, *Sol. Energy Mater. Sol. Cells*, 2006, **90**, 2011; (b) A. Ghicov and P. Schmuki, *Chem. Commun.*, 2009, 2791; (c) R. Hahn, T. Stergioulus, J. M. Macak, D. Tsoukleris, A. G. Kontos, S. P. Albu, D. Kim, A. Ghicov, J. Kunze, P. Falaras and P. Schmuki, *Phys. Status Solidi RRL*, 2007, **1**, 135; (d) K. Shankar, J. I. Basham, N. K. Allam, O. K. Varghese, G. K. Mor, X. J. Feng, M. Paulose, J. A. Seabold, K. S. Choi and C. A. Grimes, *J. Phy. Chem.C*, 2009, **113**, 6327.
- 18 (a) A. L. Yerokhin, X. Nie, A. Leyland, A. Matthews and S. J. Dowey, *Surf. Coat. Technol.*, 1999, **122**, 73-93; (b) L. H. Li, Y. M. Kong, H. W. Kim, Y. W. Kim, H. E. Kim, S. J. Heo and J. Y. Koak, *Biomaterials*, 2004, **25**, 2867; (c) Y. Han, S. H. Hong and K. W. Xu, *Surf. Coat. Technol.*, 2003, **168**, 249.
- 19 (a) Y. K. Lai, C. J. Lin, J. Y. Huang, H. F. Zhuang, L. Sun and T. Nguyen, *Langmuir*, 2008, **24**, 3867; (b) Y. K. Lai, X. F. Gao, H. F. Zhuang, J. Y. Huang, C. J. Lin and L. Jiang, *Adv. Mater.*, 2009, **21**, 3799; (c) Y. X. Tang, Y. K. Lai, D. G. Gong, K.-H. Goh, T.-T. Lim, Z. L. Dong, and Z. Chen, *Chem. Eur. J.*, 2010, **16**, 7704.
- 20 (a) G. Liu, L. Z. Wang, C. H. Sun, X. X. Yan, X. W. Wang, Z. G. Chen, S. C. Smith, H. M. Cheng and G. Q. Lu, *Chem. Mater.*, 2009, **21**, 1266; (b) T. W. Kim, S. G. Hur, S. J. Hwang, H. Park, W. Choi and J. H. Choy, *Adv. Funct.Mater.*, 2007, **17**, 307.
- 21 T. Gao, H. Fjellvag and P. Norby, *Inorg. Chem.*, 2009, **48**, 1423.
- 22 C. C. Tsai and H. S. Teng, *Chem. Mater.*, 2006, **18**, 367.
- 23 (a) D. A. Vermilyea, *Acta Metall.* 1953, **1**, 282; (b) L. Young, *Transactions of the Faraday Society*, 1954, **50**, 153.
- 24 H. M. Kim, F. Miyaji, T. Kokubo and T. Nakamura, *J. Mater. Sci. -Mater. Med.*, 1997, **8**, 341.
- 25 C. K. Lee, K. S. Lin, C. F. Wu, M. D. Lyu and C. C. Lo, *J. Hazard. Mater.*, 2008, **150**, 494.
- 26 (a) M. R. Huang, Q. Y. Peng and X. G. Li, *Chem. Eur. J.*, 2006, **12**, 4341; (b) X. J. Ju, S. B. Zhang, M. Y. Zhou, R. Xie, L. Yang and L. Y. Chu, *J. Hazard. Mater.*, 2009, **167**, 114.
- 27 (a) D. J. Yang, Z. F. Zheng, H. W. Liu, H. Y. Zhu, X. B. Ke, Y. Xu, D. Wu and Y. Sun, *J. Phys. Chem. C*, 2008, **112**, 16275; (b) H. Kochkar, A. Turki, L. Bergaoui, G. Berhault and A. Ghorbel, *J. Colloid Interface Sci.*, 2009, **331**, 27.